ACS OMEGA

http://pubs.acs.org/journal/acsodf

Article

# Hierarchical $Na_3V_2(PO_4)_2F_3$ Microsphere Cathodes for High-Temperature Li-Ion Battery Application

Partheeban Thamodaran, Vivekanantha Murugan, Devikala Sundaramurthy, Karthikeyan Sekar, Arthanareeswari Maruthapillai,* and Tamilselvi Maruthapillai*

Cite This: *ACS Omega* 2022, 7, 26523−26530

Read Online

ACCESS | Metrics & More | Article Recommendations | Supporting Information

**ABSTRACT:** Sodium superionic conductor (NASICON)-structured $Na_3V_2(PO_4)_2F_3$ cathode materials have received vast attention in the high-temperature storage performance due to their structural and thermal stability. Herein, hierarchical $Na_3V_2(PO_4)_2F_3$ microspheres (NVPF-HMSs) consisting of nanocubes were designed by a one-pot facial solvothermal method. The hierarchical $Na_3V_2(PO_4)_2F_3$ microsphere size is 2−3 $\mu$m, which is corroborated by FE-SEM and HR-TEM analyses. The NVPF-HMSs have been demonstrated as a cathode in Li-ion batteries at both low and elevated temperatures (25 and 55 °C, respectively). The NVPF-HMS cathode in a Li-ion cell exhibits reversible capacities of 119 mA h $g^{-1}$ at 0.1 C and 85 mA h $g^{-1}$ at 1 C with an 82% retention after 250 cycles at 25 °C. At elevated temperatures, the NVPF-HMS cathode exhibits a superior capacity of 110 mA h $g^{-1}$ at 1 C along with a retention of 90% after 150 cycles at 55 °C. Excellent capacity and cyclability were achieved at 55 °C due to its hierarchical morphology with a robust crystal structure, low charge-transfer resistance, and improved ionic diffusivity. The Li-ion storage performance of the NVPF-HMS cathode material at elevated temperatures was analyzed for the first time to understand the high-temperature storage property of the material, and it was found to be a promising candidate for elevated-temperature energy storage applications.

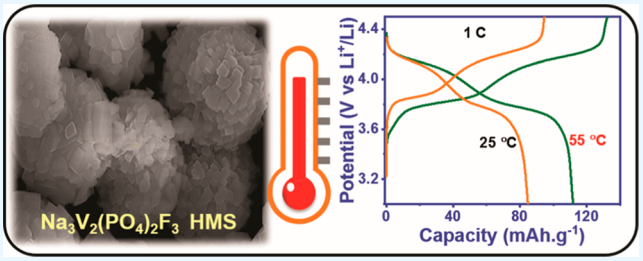


## 1. INTRODUCTION

Li-ion batteries have received great attention over the world as leading energy storage technologies in modern society and are widely used in various portable and hybrid electronic vehicles. Li-ion batteries possess high voltage, high energy density, and long durability compared to other secondary batteries.[1−3] Notably, cathodes have considerably influenced the overall Li-ion battery performance. Therefore, various cathode candidates ($LiCoO_2$, NMC, and $LiMn_2O_4$) have been extensively studied and commercialized in LIBs.[4] However, there remains a huge challenge to achieve high-power, high-energy Li-ion batteries.[5] In addition, cathode materials are facing serious problems in terms of capacity decay and thermal runway when cycled at a higher temperature. Hence, the development of high-temperature-tolerant cathodes is critical for the success of next-generation Li-ion battery applications.[6,7]

Recently, vanadium-based fluorophosphate ($Na_3V_2(PO_4)_2F_3$) with a sodium superionic conductor (NASICON) framework compound has been found to be a promising cathode in $Na^+$ or $Li^+$ ion storage as it is thermally stable and has high structural stability, excellent electrical conductivity, and ionic transport.[8,9] le Meins et al., in 1999, described the structural features of $Na_3V_2(PO_4)_2F_3$ crystals with tetragonal symmetry (space group of $P4_2/mnm$).[10] Hence, the sodium storage performance of $Na_3V_2(PO_4)_2F_3$ materials has been systematically explored and they exhibit a capacity of 110−120 mA h $g^{-1}$ at a voltage of 3.6 V.[11] Besides, the attractive crystal structure of $Na_3V_2(PO_4)_2F_3$ showed exceptional performances as a cathode material in Li-ion batteries. Barker et al., in 2006, demonstrated the use of $Na_3V_2(PO_4)_2F_3$ as the cathode material for a Li-ion battery conventionally with a Li-based electrolyte, while graphite was used as the anode.[12,13] Electrochemical $Na^+/Li^+$ ion-exchange mechanisms during electrochemical studies were realized by Song et al. 2014.[14] The $Na_3V_2(PO_4)_2F_3$ cathode adapts the same chemistry in Li-ion batteries like Na-ion batteries, where Li ions are exchanged with host $Na^+$ ions for few cycles, and subsequently, predominant Li-ion shuttling occurs, resulting in hybrid-ion batteries.[14] Moreover, electrochemical ion exchange of $Na^+/Li^+$ results in $Na_{3-x}Li_xV_2(PO_4)_2F_3$ formation, which has been discussed in detail in the previous report.[15] However, the $Na_3V_2(PO_4)_2F_3$ cathode has limited reversible capacity due to poor electronic conductivity and diffusivity. In this

Received: April 26, 2022
Accepted: June 29, 2022
Published: July 22, 2022

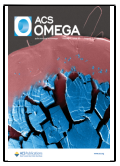

Scheme 1. Schematic Representation of the Synthesis of NVPF-HMSs

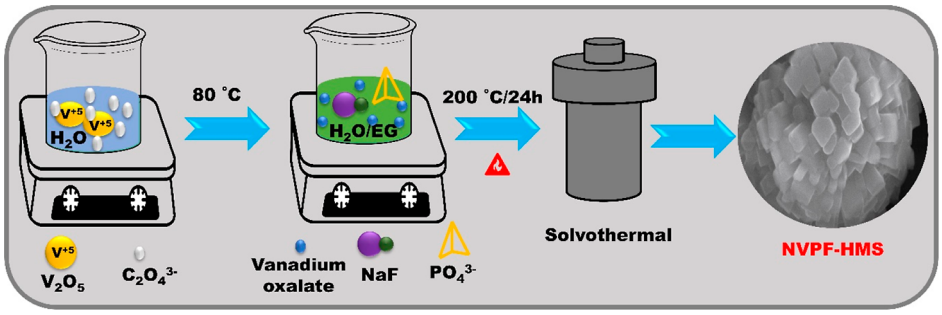


perspective, many strategies have been followed to improve the electrochemical performance such as carbon coating, metal ion doping, design of nanoarchitecture materials, and so forth.[16,17]

Notably, dimension, texture properties, and morphologies have strongly influenced the electrochemical performance of $Na_3V_2(PO_4)_2F_3$ in energy storage applications. Until now, diverse morphologies of the $Na_3V_2(PO_4)_2F_3$ cathode, including nanowires, nanoflowers, nano-/microcubes, and microspheres have been explored in Na-ion batteries.[18−21] Recently, Fang et al., in 2022, reported morphological impact on $Na_3V_2(PO_4)_2F_3$ cathode performances for Na-ion batteries.[22] The micro-/nanostructure morphology of the $Na_3V_2(PO_4)_2F_3$ cathode designed by one-pot hydro-/solvothermal method without any high-temperature treatment has received great attention as it reduces the time, energy, and controls the particle size.[23,24] Recently, the synthesis of hierarchical micro-/nanostructures of $Na_3V_2(PO_4)_2F_3$ morphology has attracted attention for designing Li-/Na-ion batteries due to their extraordinary properties that suppress particle agglomeration; low volume expansion leads to better electrical conductivity and diffusivity.[25,26] Based on reports, direct synthesis of Li analogues of $Na_3V_2(PO_4)_2F_3$ with a nano-/microstructure has been challenging due to impurity formation.[26] Recently, Mukherjee et al., in 2020, prepared a Li analogue of $Na_{0.7}Li_{2.3}V_2(PO_4)_2F_3$ hierarchical hollow microspheres from $Na_3V_2(PO_4)_2F_3$ by the ion-exchange method and utilized it as a cathode for Li-ion battery applications.[26] Very few reports produced $Na_3V_2(PO_4)_2F_3$ with a hierarchical micro-/nanostructure morphology for Li-ion battery applications.[26] Previously, Essehli et al., in 2020, reported the nanorod morphology of the $Na_3V_2(PO_4)_2F_3$ @MWCNT cathode for a Na-ion battery studied at high temperatures.[27]

Herein, we attempted a one-pot solvothermal approach for the construction of a $Na_3V_2(PO_4)_2F_3$ hierarchical microsphere (NVPF-HMS) cathode for Li-ion batteries. Furthermore, the impact of temperature on Li storage in NVPF-HMSs was extensively investigated at ambient to higher temperatures. The hierarchical microspheres consisting of nanocubes significantly enhanced the electrical conductivity, leading to Li-ion diffusion and resulting in higher capacity and stability at an elevated temperature (55 °C) compared with those at room temperature.

## 2. EXPERIMENTAL SECTION

In a typical synthesis of NVPF-HMSs (Scheme 1), a vanadium oxalate solution was prepared by dissolving a 1:3 ratio of $V_2O_5$ (1 mmol) and oxalic acid in 30 mL of DI water at 80 °C for 20 min under vigorous stirring. After cooling the above solution to room temperature, 30 mL of ethylene glycol (EG) was poured to obtain a green solution. Subsequently, a stoichiometric mixture of sodium fluoride (3 mmol) and ammonium dihydrogen phosphate (2 mmol) was added under stirring conditions and then allowed to continue for 20 min. Afterward, the solution was poured into a Teflon-lined autoclave with a stainless-steel cover and heat-treated at 200 °C for 24 h in an oven. The obtained precipitate was filtered and washed with ethanol and DI water. The filtered product was dried in an oven at 80 °C for 12 h, and a light-green final product was obtained, which was used without any further high-temperature treatment.

**2.1. Material Characterization.** Powder X-ray diffraction analysis was carried out using Bruker (D8 ADVANCE, Da Vinci) analytical instruments with a Cu K$\alpha$ radiation source (1.54 Å) to understand the crystal structure of the synthesized material. The X-ray diffraction (XRD) data was recorded in the $2\theta$ range of 10−80° at a scan speed of 3° $min^{-1}$ with a 0.04 step size. The surface morphology of the as-prepared material was observed using field emission scanning electron microscopy (ZEISS operated at 10 kV). High-resolution transmission electron microscopy (JEOL JEM-2010 at an accelerated voltage of 200 kV) was performed to understand the morphology and crystallinity of the synthesized material. The oxidation state of the material was identified by X-ray photoelectron spectroscopy (1032 instrument with Al-alpha).

**2.2. Electrochemical Characterization.** Electrochemical studies of the synthesized NVPF-HMS materials were carried out using CR-2032 coin-type cells in the half-cell configuration. To fabricate the working electrode, a mixture of NVPF-HMS materials, Super-P carbon, and PVDF binder in the weight ratio of 75:20:5 with *N*-methyl pyrrolidine solvent was used. The slurry was coated on an aluminum current collector using the doctor-blade technique and dried at 100 °C for 12 h in a vacuum oven and then roll-pressed. The resulting electrode film was cut into a round disk 15 mm in diameter with a material loading of 3.0 mg/$cm^2$. 1.0 M $LiPF_6$ dissolved in ethylene carbonate and dimethylene carbonate in the ratio of 1:1 (EC/DMC) was used as an electrolyte solution. The coin cell consisted of a working electrode against a Li-metal reference electrode, separated by Whatman glass microfibers soaked with few drops of the electrolyte solution. The CR-2032 coin-type cell was assembled inside an argon gas-filled glovebox (MBraun GmbH, Germany) maintained under less than 0.5 ppm of oxygen and moisture level. Cyclic voltammetry and galvanostatic charge/discharge were carried out using the Biologic instrument BCS 810 series. Cyclic voltammetry was performed in the voltage range of 3.0−4.5 V at a scan rate of 0.2 mV/s. Galvanostatic electrochemical impedance spectra were obtained using a VSP-300 workstation in the frequency range from 100 kHz to 10 MHz at a 10 mA


https://doi.org/10.1021/acsomega.2c02558
ACS Omega 2022, 7, 26523−26530

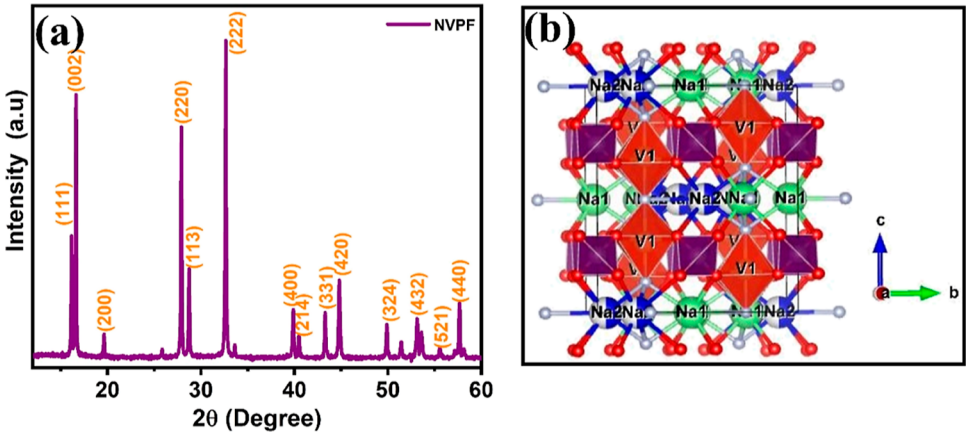


**Figure 1.** (a) Powder XRD pattern of NVPF-HMS and (b) crystal structure of NVPF.

amplitude. An elevated temperature (55 °C)-dependent electrochemical study was carried out using an ESPEC-SH222 tabletop humidity chamber.

## 3. RESULTS AND DISCUSSION

The diffraction peaks of NVPF-HMS samples from the XRD pattern revealed tetragonal symmetry ($P4_2/mnm$), as confirmed from the JCPDS card data (01-089-8485).[19] Highly crystalline peaks and pure phase NVPF-HMS formation without any impurities are presented in Figure 1a. The lattice parameters and cell volume of NVPF-HMS were found to be $a$ = 9.04, $b$ = 9.04, and $c$ = 10.70 Å and 876.9 Å$^3$, respectively.[8] The crystal structure of NVPF is depicted in Figure 1b, and as shown, the $V_2O_8F_3$ bi-octahedron and $PO_4$ tetrahedron are arranged in a three-dimensional network with two interstitial tunnel sites named Na (1) and Na (2). Furthermore, fully occupied Na (1) sites and half-occupied Na (2) sites are seen in the network.

The $Na^+$ ions in Na (2) sites are exchanged with $Li^+$ during electrochemical cycling due to less energy compared with the Na (1) site. The NASICON crystal structure of NVPF-HMSs could provide 3D channels through the $a-b$ plane for Li-ion migration. Moreover, the smaller the size of the Li ion, the more easily it accesses the Na host site, resulting in excellent electrochemical performance.

Three-dimensional images of NVPF-HMS materials were imaged by FE-SEM analysis, which confirmed the hierarchical microsphere (Figure 2a) with a size range of 2−3 $\mu$m. Furthermore, each microsphere is assembled from hierarchical microflowers with smaller nanocubes with a size of ∼200 nm (Figure 2b). The hierarchical microsphere consists of nanocubes derived from the Ostwald ripening process, where smaller particles are recrystallized over larger particles under solvothermal conditions. Earlier, sheet- and needle-aggregated hierarchical hollow structures of NVPF were derived by the two-step solvothermal method.[25]

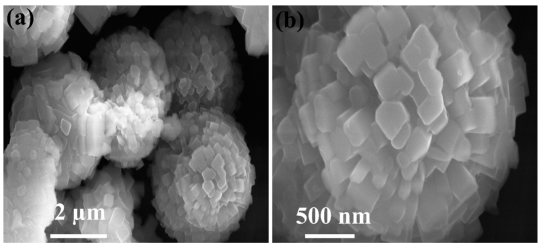


**Figure 2.** (a,b) Low−high magnification FE-SEM images of NVPF-HMSs.

Interestingly, we observed cubes aggregated on the microspheres of NVPF by a simple one-step solvothermal method. Notably, the mixed solvent of ethylene glycol/water promoted the NVPF seed crystal and further the growth of hierarchical microspheres with aggregated nanocubes. However, irregular morphology of NVPF was observed when water or EG alone was used as a reaction medium; the corresponding FE-SEM images are displayed in Figure S1a,b. The hierarchical microsphere has a nanocube morphology, and it favors the facile electrical and ionic conductivity of the NVPF materials in the three-dimensional pathway. The approximate chemical composition of NVPF-HMS was confirmed by energy-dispersive X-ray spectrometry (EDX) analysis presented in Figure S2. The hierarchical microspheres consist of nanocubes of NVPF, which is further verified by HR-TEM analysis, as displayed in Figure 3. The hierarchical microspheres of NVPF (Figure 3a) with an average size of 2−3 $\mu$m are very obvious, and each microsphere is formed by the self-assembly of nanocubes with a size of 200 nm (Figure 3b). The HR-TEM (Figure 3c) image clearly indicated the hierarchical growth of nanocubes in the presence of ethylene glycol/water under solvothermal conditions. Figure 3d shows the selected-area electron diffraction (SAED) pattern of NVPF-HMS, which reveals the highly crystalline property of NVPF-HMS materials. Tap density is one of the important properties of electrode materials, which depends on the surface structure, morphology, and size of the particles.[28] The tap density of NVPF-HMSs and other reported materials such as irregular particle[13] and microsphere[18] morphologies of NVPF was measured by the mass-to-unit volume ratio method. Among them, the NVPF-HMSs (1.1 g/cm$^3$) have a significantly higher tap density compared with irregular particles (0.85 g/cm$^3$) and microspheres (0.92 g/cm$^3$). The achieved higher tap density of NVPF-HMSs is due to the hierarchical microstructure with a nanocube morphology, and it provides high packing density in the electrode and better electrochemical performance.

XPS analysis was performed to obtain insight into the surface elemental composition and the oxidation states of the NVPF-HMS material. Figure 4a depicts a survey scan of the NVPF-HMS material, which clearly demonstrates the existence of V 2p, P 2p, O 1s, F 1s, and Na 1s elements in the material. Figure 4b displays the V 2p XPS spectra of NVPF-HMSs and


https://doi.org/10.1021/acsomega.2c02558
ACS Omega 2022, 7, 26523−26530

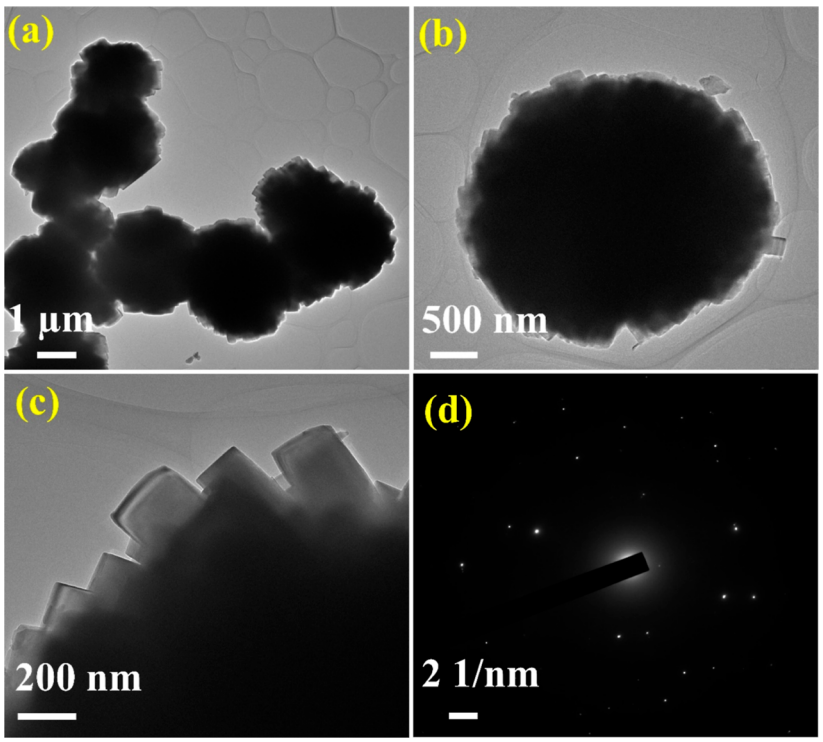


**Figure 3.** (a,b) Low–high magnification HR-TEM images of NVPF-HMSs, (c) high-resolution image, and (d) SAED pattern.

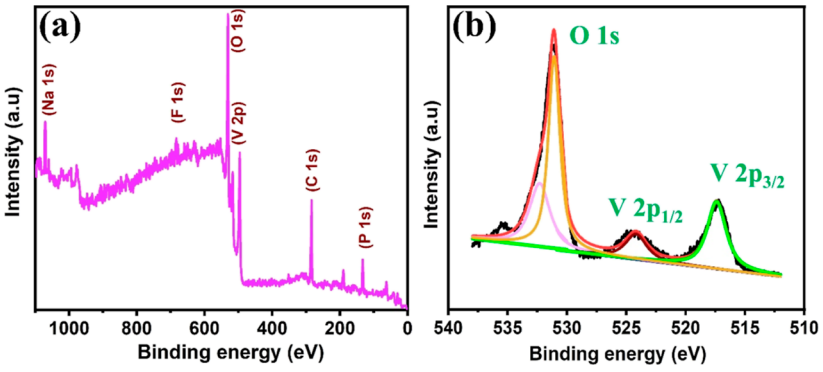


**Figure 4.** (a) Survey spectra and (b) vanadium 2p and oxygen 1s peaks of NVPF-HMSs.

exhibits two binding energies of 517.2 and 524.1 eV, which could be assigned to V $2p_{3/2}$ and V $2p_{1/2}$, respectively, in the form of $V^{3+}$ in the NVPF-HMS material. Furthermore, the binding peak at 530 eV corresponds to the O 1s peak of NVPF-HMSs.

**3.1. Electrochemical Studies.** The storage performance of the NVPF-HMS cathode-constructed Li-ion battery was evaluated at room temperature (25 °C), and the results are presented in Figure 5. The cyclic voltammetry (CV) profiles at a sweep rate of 0.2 mV $s^{-1}$ show two oxidation peaks appearing during anodic scan at 3.92 and 4.21 V attributed to the extraction of $Na^+$ ions at two different sites Na (2) and Na (1), respectively, as displayed in Figure 5a. In the reverse scan, the formation of two reduction peaks around 4.07 and 3.75 V is assigned to $Li^+$ insertion instead of $Na^+$ and is also known as the hybrid-ion process, which is in good agreement with the literature system.[14] Furthermore, the consecutive CV traces overlapped and peaks separated well, which is indexed to the highly reversible kinetics of the NVPF-HMS electrode in Li-ion batteries.

Figure 5b shows the galvanostatic charge–discharge curve of the NVPF-HMS cathode measured at 0.1 C in the voltage window of 3–4.5 V at 25 °C. The NVPF-HMSs exhibit discharge capacities of 119, 115, 112, 110, and 110 mA h $g^{-1}$ in the 1st, 10th, 50th, 80th, and 100th cycles, respectively, with a 92% capacity retention. Furthermore, the charge/discharge curve shows a couple of redox plateaus at ∼3.83/3.79 and ∼4.17/4.13 V (vs $Li^+$/Li), which is in good agreement with the above CV studies. The average discharge voltage of NVPF-HMSs is close to ∼4 V, which is greater than that of other NASICON-based cathode materials with a similar redox couple of $V^{3+}/V^{+4}$ versus $Li^+$/Li, such as $Li_3V_2(PO_4)_3$ (∼3.8 V)[29] and $NaLi_2V_2(PO_4)_3$ (∼3.7 V).[30] The high voltage of fluorophosphate materials, owing to the inductive effect of fluorine, thus enhances the energy of the vanadium redox center.[8] Interestingly, the electrochemical performance of NVPF-HMSs is superior compared with that of other reported nanostructure morphologies of NVPF in Li-ion batteries, as shown in Table S1. This reveals that the NVPF-HMSs exhibit higher capacity and retention compared with other nanostruc-


https://doi.org/10.1021/acsomega.2c02558
ACS Omega 2022, 7, 26523–26530

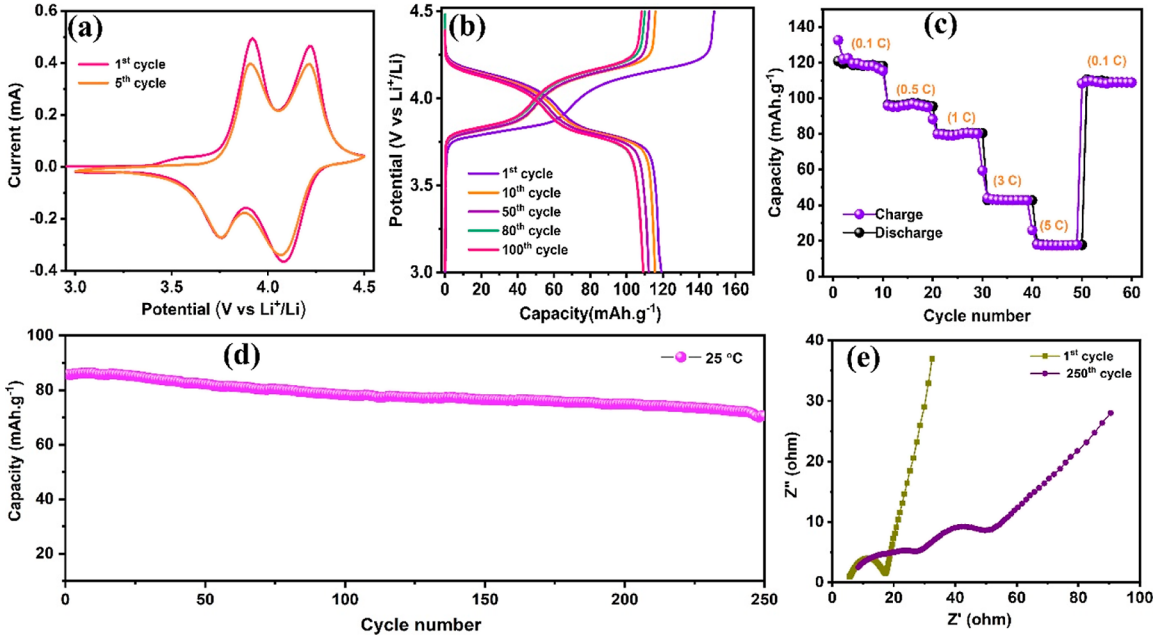


**Figure 5.** Electrochemical performance of the NVPF-HMS cathode at 25 °C; (a) CV profile at 0.2 mV $s^{-1}$, (b) galvanostatic charge−discharge curve at 0.1 C, (c) rate performance at different C values, (d) long cycle performance at 1 C, and (e) EIS spectra.

ture-based NVPF materials. This impressive performance along with high capacity and good retention achieved because of the hierarchical architecture of the NVPF-HMS cathode offers facile electrical conductivity and Li-ion transport. The rate capability of the NVPF-HMS electrode was measured at different current densities, as presented in Figure 5c. It reveals that the NVPF-HMS cathode at 0.1, 0.5, 1.0, 3.0, and 5.0 C delivered discharge capacities of 119, 95, 80, 40, and 20 mA h $g^{-1}$, respectively. Moreover, the capacity value narrows down upon an increase in the current density. Albeit, the NVPF-HMS cathode regained its original capacity after returning to a lower current rate of 0.1 C, suggesting high electrode reversibility and good rate capability of electrode materials. The long-term durability of the NVPF-HMS cathode was investigated at 1 C in the voltage range of 3−4.5 V at 25 °C. The plot of discharge capacity versus the cycle number displayed in Figure 5d indicates that the NVPF-HMS cathode delivered an initial capacity of 85 mA h $g^{-1}$ with an 82% retention after 250 cycles. In addition, the NVPF-HMS electrode exhibited excellent capacity because the hierarchical microspheres consist of nanocubes which enhance its electrochemical properties. The NVPF-HMSs have a large specific surface area, which enables a better electrode/electrolyte contact and faster lithium insertion/extraction. Furthermore, due to the low volume change and distortion of the crystal structure during charge/discharge investigation, improved Li-ion diffusion can be accomplished. However, capacity decay was observed after prolonged cycling studies owing to a decrease of the electrical conductivity and degradation of original materials. Investigation of the electrode kinetics of NVPF-HMSs was conducted by EIS analysis during the 1st and after the 250th cycles at 1 C, and the corresponding Nyquist plots are shown in Figure 5e. It is worth noting that the semicircle at the higher-frequency region is related to charge-transfer impedance ($R_{ct}$), while the low-frequency Warburg line is assigned to Li-ion diffusion in the active electrode material. In the EIS spectra, the lower $R_{ct}$ value in the initial cycle is attributed to the NVPF electrode possessing high electrical conductivity. However, after cycling, the charge-transfer resistance increased and one more semicircle became visible in the middle-frequency region, which accounts for the formation of solid−electrolyte interphase growth. Therefore, electrical conductivity decreases and causes Li-ion diffusion, which reflects capacity decay after prolonged cycles.

The circuit-fitted EIS spectra of the NVPF-HMS electrode during the 1st and after the 250th cycles are displayed in Figure S3a. In the figure, $R_s$ corresponds to the Ohmic resistance of the electrolyte, $R_{ct}$ refers to the charge-transfer resistance, and $C_{dl}$ and $Z_w$ are related to the diffusion of $Li^+$ ions via the electrode/electrolyte interface. The Li-ion diffusion coefficient of the NVPF-HMS cathode was calculated using the Nyquist plot and eqs 1 and 2.

$$Z' = R_s + R_{ct} + \sigma\omega^{-1/2} \quad (1)$$

$$D_{Li^+} = R^2T^2/2A^2n^4C^2F^4\sigma^2 \quad (2)$$

where $Z'$ is the real impedance, $R_s$ is the solution resistance, $D_{Li^+}$ is the Li-ion diffusion coefficient, $R$ is the gas constant, $T$ is the absolute temperature, $A$ is the electrode surface area, $n$ is the number of electrons transferred, $F$ is the Faraday constant, $C$ is the concentration of $Li^+$, and $\sigma$ is the Warburg factor. The "$\sigma$" is derived from a linear plot between the real impedance ($Z'$) and angular frequency ($\omega^{-1/2}$) in the low-frequency region according to eq 1. The fitted linear plot of NVPF-HMSs in the 1st and after the 250th cycles under 25 °C is displayed in Figure S3b. $D_{Li^+}$ was calculated using eq 2, and the Li-ion diffusion values of NVPF-HMSs are $3.5 \times 10^{-10}$ and $2.0 \times 10^{-10}$ $cm^2$ $s^{-1}$ in the 1st and after the 250th cycles, respectively, which are comparable with the reported literature.[31,32] Moreover, the NVPF-HMSs exhibit high Li-ion diffusion in the initial cycle owing to their hollow morphology and NASICON structure with 3D ion transport, resulting in excellent kinetics of Li-ion diffusion. However, Li-ion diffusivity decreased after the 250th cycle as the structure


https://doi.org/10.1021/acsomega.2c02558
ACS Omega 2022, 7, 26523−26530

and morphology were not stable, which resulted in capacity decay after prolonged cycles.

High-temperature performance of the NVPF-HMS cathode was explored in Li-ion batteries at 1 C and 55 °C. The 1st and 150th galvanostatic charge/discharge curves of the NVPF-HMS cathode are displayed in Figure 6a. As shown, the NVPF-

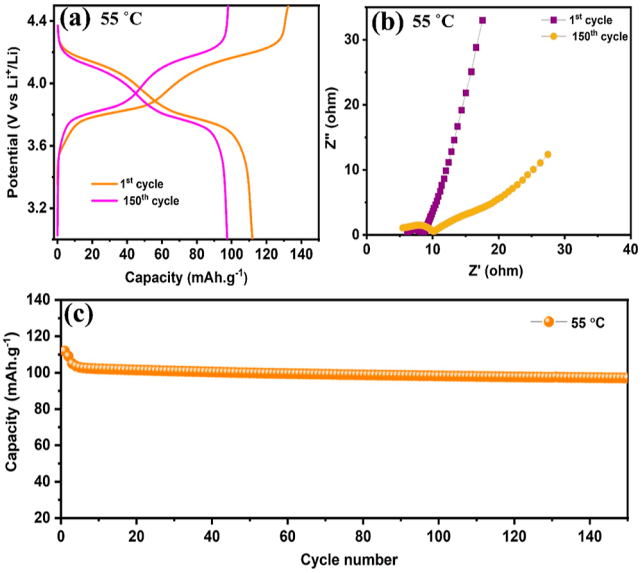


**Figure 6.** Electrochemical performance of the NVPF-HMS cathode at 55 °C, (a) galvanostatic charge−discharge curve at 1 C, (b) EIS spectra, and (c) long cycle performance at 1 C.

HMS cathode exhibits a capacity of 110 mA h $g^{-1}$ at 1 C with a retention capacity of 90% during the 150th cycle. At 55 °C, the cycled cell exhibits high capacity and cyclability because of its hierarchical structure with robust crystal nature and enhanced ionic and electronic conductivity. Further EIS analysis of the NVPF-HMS cathode-assembled cell was carried out during the initial (1st) cycle and after the 150th cycle at 1 C under 55 °C, as displayed in Figure 6b. The EIS spectra show lower charge-transfer resistance ($R_{ct}$) for the freshly prepared cell at 55 °C, which resulted in higher electrical and ionic diffusivity, leading to better electrochemical performance. The charge-transfer resistance slightly increased after 150 cycles, but stable performance observed due to high electrical conductivity was related to electrode stability at 1 C and 55 °C. Figure 6c shows the long-term cycling of the NVPF-HMS cathode in the Li cell at 1 C under 55 °C, further confirming excellent durability for a long term with 90% retention after 150 cycles. The NVPF-HMSs delivered high capacity and excellent cycling performance at 1 C under 55 °C due to their robust structure and lower charge-transfer resistance, leading to enhanced electrical conductivity and ionic diffusivity.

The circuit-fitted EIS spectra of the NVPF-HMS electrode in the 1st cycle and after the 150th cycle are displayed in Figure S4a. In the figure, $R_s$ corresponds to the Ohmic resistance of the electrolyte, $R_{ct}$ refers to the charge-transfer resistance, and $C_{dl}$ and $Z_w$ are related to the diffusion of $Li^+$ ions via the electrode/electrolyte interface. The Li-ion diffusion coefficient of the NVPF-HMS electrode is measured during the 1st cycle and after the 150th cycle under 55 °C using eq 2, where $\sigma$ is obtained from the linear plot between real impedance ($Z'$) and angular frequency ($\omega^{-1/2}$) in the low-frequency region (Figure S4b). Furthermore, the measured Li-ion diffusivity of NVPF-HMS is $5.2 \times 10^{-10}$ and $4.5 \times 10^{-10}$ $cm^2$ $s^{-1}$ for the 1st and 150th cycled electrode, respectively. The high Li-ion diffusivity observed during the 1st cycle, owing to the hierarchical morphology and faster Li-ion transport, thereby enhances the reaction kinetics and the overall electrochemical performance. Furthermore, the diffusion value does not deviate significantly after the 150th cycle, indicating that the electrode materials are more stable even after prolonged cycles at higher current rates.

## 4. CONCLUSIONS

We have demonstrated a one-step solvothermal method for the synthesis of NVPF-HMSs using ethylene glycol/water in the reaction medium. The XRD, FE-SEM, and HR-TEM characterizations corroborated tetragonal symmetry and a hierarchical microsphere morphology with the size ranging from 2 to 3 $\mu$m. The NVPF-HMS cathode was constructed in a Li-ion battery, and the performances were measured both at room and elevated temperatures. As a result, a reversible capacity of 119 mA h $g^{-1}$ at 0.1 C and a capacity of 85 mA h $g^{-1}$ at 1 C with an 82% retention after 250 cycles at 25 °C were observed. Moreover, an extraordinary capacity of 110 mA h $g^{-1}$ at 1 C with a retention of 90% in the 150th cycle was achieved at 55 °C. An excellent capacity and stability were achieved at a high temperature of 55 °C due to the highly crystal structure, low charge-transfer resistance, and enhanced electrical and ionic conductivity.

## ■ ASSOCIATED CONTENT

### Supporting Information

The Supporting Information is available free of charge at https://pubs.acs.org/doi/10.1021/acsomega.2c02558.

Different solvent-mediated synthesis of NVPF: water and EG; EDX profile of NVPF-HMS, electrochemical performance of NVPF-HMS compared with other reported NVPF for Li-ion battery applications; equivalent circuit and linear fitted plot between $Z'$ and $\omega^{-1/2}$ of NVPF-HMSs in the 1st and 250th cycles at room temperature (25 °C); and equivalent circuit and linear fitted plot between $Z'$ and $\omega^{-1/2}$ of NVPF-HMSs in the 1st and 150th cycles at a high temperature (55 °C) (PDF)

## ■ AUTHOR INFORMATION


### Corresponding Authors

**Arthanareeswari Maruthapillai** − *Department of Chemistry, College of Engineering and Technology, SRM Institute of Science and Technology, Kattankulathur, Tamil Nadu 603203, India;* orcid.org/0000-0002-1794-3967; Phone: +91-9600112945; Email: tamilselvi.marudhapillai@gmail.com

**Tamilselvi Maruthapillai** − *Thiru Kolanjiappar Government Arts College, Virudhachalam, Tamil Nadu 606001, India;* Email: arthanareeswari@gmail.com

### Authors

**Partheeban Thamodaran** − *Department of Chemistry, College of Engineering and Technology, SRM Institute of Science and Technology, Kattankulathur, Tamil Nadu 603203, India*

**Vivekanantha Murugan** − *Department of Physics and Nanotechnology, College of Engineering and Technology,*




https://doi.org/10.1021/acsomega.2c02558
ACS Omega 2022, 7, 26523−26530

*SRM Institute of Science and Technology, Kattankulathur, Tamil Nadu 603203, India*

**Devikala Sundaramurthy** − *Department of Chemistry, College of Engineering and Technology, SRM Institute of Science and Technology, Kattankulathur, Tamil Nadu 603203, India;* orcid.org/0000-0002-1224-0947

**Karthikeyan Sekar** − *Department of Chemistry, College of Engineering and Technology, SRM Institute of Science and Technology, Kattankulathur, Tamil Nadu 603203, India;* orcid.org/0000-0002-3422-8009

Complete contact information is available at: https://pubs.acs.org/10.1021/acsomega.2c02558

### Notes

The authors declare no competing financial interest.

## ■ ACKNOWLEDGMENTS

The authors would like to thank the Department of Chemistry at the SRMIST. The authors thank the SRM SCIF and Nanotechnology Research Centre, SRMIST, for providing facilities for FE-SEM and HR-TEM analysis. The first author thanks the Council of Scientific and Industrial Research (CSIR) for providing the Senior Research Fellowship (SRF).

## ■ REFERENCES

(1) Armand, M.; Tarascon, J.-M. Building better batteries. *Nature* **2008**, *451*, 652−657.

(2) Yoo, H. D.; Markevich, E.; Salitra, G.; Sharon, D.; Aurbach, D. On the Challenge of Developing Advanced Technologies for Electrochemical Energy Storage and Conversion. *Mater. Today* **2014**, *17*, 110−121.

(3) Tarascon, J.-M.; Armand, M. Issues and Challenges Facing Rechargeable Lithium Batteries. *Nature* **2001**, *414*, 359−367.

(4) Manthiram, A. A Reflection on Lithium-Ion Battery Cathode Chemistry. *Nat. Commun.* **2020**, *11*, 1550.

(5) Goodenough, J. B.; Kim, Y. Challenges for Rechargeable Li Batteries. *Chem. Mater.* **2010**, *22*, 587−603.

(6) Chu, C.-T.; Mondal, A.; Kosova, N. V.; Lin, J.-Y. Improved High-Temperature Cyclability of $AlF_3$ Modified Spinel $Li-Ni_{0.5}Mn_{1.5}O_4$ Cathode for Lithium-Ion Batteries. *Appl. Surf. Sci.* **2020**, *530*, 147169.

(7) Hou, J.; Yang, M.; Wang, D.; Zhang, J. Fundamentals and Challenges of Lithium Ion Batteries at Temperatures between −40 and 60 °C. *Adv. Energy Mater.* **2020**, *10*, 1904152.

(8) Shakoor, R. A.; Seo, D.-H.; Kim, H.; Park, Y.-U.; Kim, J.; Kim, S.-W.; Gwon, H.; Lee, S.; Kang, K. A Combined First Principles and Experimental Study on $Na_3V_2(PO_4)_2F_3$ for Rechargeable Na Batteries. *J. Mater. Chem.* **2012**, *22*, 20535.

(9) Kosova, N. V.; Rezepova, D. O. Mixed Sodium-Lithium Vanadium Fluorophosphates $Na_{3-X}Li_xV_2(PO_4)_2F_3$: The Origin of the Excellent High-Rate Performance. *J. Power Sources* **2018**, *408*, 120−127.

(10) le Meins, J.-M.; Crosnier-Lopez, M.-P.; Hemon-Ribaud, A.; Courbion, G. Phase Transitions in the $Na_3M_2(PO_4)_2F_3$ Family ($M=Al^{3+}$, $V^{3+}$, $Cr^{3+}$, $Fe^{3+}$, $Ga^{3+}$): Synthesis, Thermal, Structural, and Magnetic Studies. *J. Solid State Chem.* **1999**, *148*, 260−277.

(11) Zhu, L.; Wang, H.; Sun, D.; Tang, Y.; Wang, H. A Comprehensive Review on the Fabrication, Modification and Applications of $Na_3V_2(PO_4)_2F_3$ Cathodes. *J. Mater. Chem. A* **2020**, *8*, 21387−21407.

(12) Gover, R.; Bryan, A.; Burns, P.; Barker, J. The Electrochemical Insertion Properties of Sodium Vanadium Fluorophosphate, $Na_3V_2(PO_4)_2F_3$. *Solid State Ionics* **2006**, *177*, 1495−1500.

(13) Gover, R.; Bryan, A.; Burns, P.; Barker, J. The electrochemical insertion properties of sodium vanadium fluorophosphate, $Na_3V_2(PO_4)_2F_3$. *Solid State Ionics* **2006**, *177*, 1495−1500.

(14) Song, W.; Ji, X.; Chen, J.; Wu, Z.; Zhu, Y.; Ye, K.; Hou, H.; Jing, M.; Banks, C. E.; Banks, C. E. Mechanistic investigation of ion migration in $Na_3V_2(PO_4)_2F_3$ hybrid-ion batteries. *Phys. Chem. Chem. Phys.* **2015**, *17*, 159−165.

(15) Xiong, H.; Liu, Y.; Shao, H.; Yang, Y. Understanding the Electrochemical Mechanism of High Sodium Selective Material $Na_3V_2(PO_4)_2F_3$ in $Li^+/Na^+$ Dual-Ion Batteries. *Electrochim. Acta* **2018**, *292*, 234−246.

(16) Liu, Q.; Wang, D.; Yang, X.; Chen, N.; Wang, C.; Bie, X.; Wei, Y.; Chen, G.; Du, F. Carbon-Coated $Na_3V_2(PO_4)_2F_3$ Nanoparticles Embedded in a Mesoporous Carbon Matrix as a Potential Cathode Material for Sodium-Ion Batteries with Superior Rate Capability and Long-Term Cycle Life. *J. Mater. Chem. A* **2015**, *3*, 21478−21485.

(17) Olchowka, J.; Nguyen, L. H. B.; Broux, T.; Sanz Camacho, P.; Petit, E.; Fauth, F.; Carlier, D.; Masquelier, C.; Croguennec, L. Aluminum Substitution for Vanadium in the $Na_3V_2(PO_4)_2F_3$ and $Na_3V_2(PO_4)_2FO_2$ Type Materials. *Chem. Commun.* **2019**, *55*, 11719−11722.

(18) Mukherjee, A.; Sharabani, T.; Sharma, R.; Okashy, S.; Noked, M. Effect of Crystal Structure and Morphology on $Na_3V_2(PO_4)_2F_3$ Performances for Na-Ion Batteries. *Batteries Supercaps* **2020**, *3*, 510−518.

(19) Qi, Y.; Mu, L.; Zhao, J.; Hu, Y.-S.; Liu, H.; Dai, S. PH-Regulative Synthesis of Na3 $(VPO_4)_2F_3$ Nanoflowers and Their Improved Na Cycling Stability. *J. Mater. Chem. A* **2016**, *4*, 7178−7184.

(20) Partheeban, T.; Senthilkumar, B.; Aravindan, V.; Madhavi, S.; Sasidharan, M. Binary NaCl−NaF and NaCl−LiF Flux-Mediated Growth of Mixed-Valence $(V^{3+/4+})$ NASICON-Type $Na_3V_2(PO_4)_2F_{2.5}O_{0.5}$ and $Na_{2.4}Li_{0.6}V_2(PO_4)_2F_{2.5}O_{0.5}$ for Highly Reversible Na- and Li-Ion Storage. *ACS Appl. Energy Mater.* **2021**, *4*, 1387−1397.

(21) Li, W.; Yao, Z.; Zhang, S.; Wang, X.; Xia, X.; Gu, C.; Tu, J. High-Performance $Na_3V_2(PO_4)_2F_{2.5}O_{0.5}$ Cathode: Hybrid Reaction Mechanism Study via Ex-Situ XRD and Sodium Storage Properties in Solid-State Batteries. *Chem. Eng. J.* **2021**, *423*, 130310.

(22) Fang, R.; Olchowka, J.; Pablos, C.; Camacho, P. S.; Carlier, D.; Croguennec, L.; Cassaignon, S. Effect of the Particles Morphology on the Electrochemical Perrformance of $Na_3V_2(PO_4)_2F_{3-y}O_y$. *Batteries Supercaps* **2022**, *5*, No. e202100179.

(23) Qi, Y.; Mu, L.; Zhao, J.; Hu, Y. S.; Liu, H.; Dai, S. Superior Na-Storage Performance of Low-Temperature-Synthesized $Na_3(VO_{1-x}PO_4)_2F_{1+2x}(0 \le x \le 1)$ Nanoparticles for Na-Ion Batteries. *Angew. Chem.* **2015**, *127*, 10049−10054.

(24) Zhao, J.; Mu, L.; Qi, Y.; Hu, Y.-S.; Liu, H.; Dai, S. A Phase-Transfer Assisted Solvo-Thermal Strategy for Low-Temperature Synthesis of $Na_3(VO_{1-x}PO_4)_2F_{1+2x}$ Cathodes for Sodium-Ion Batteries. *Chem. Commun.* **2015**, *51*, 7160−7163.

(25) Du, P.; Mi, K.; Hu, F.; Jiang, X.; Wang, D.; Zheng, X. Hierarchical Hollow Microspheres $Na_3V_2(PO_4)_2F_3$ C@rGO as High-Performance Cathode Materials for Sodium Ion Batteries. *New J. Chem.* **2020**, *44*, 12985−12992.

(26) Mukherjee, A.; Sharabani, T.; Perelshtein, I.; Noked, M. High-Rate $Na_{0.7}Li_{2.3}V_2$ $(PO_4)_2F_3$ Hollow Sphere Cathode Prepared via a Solvothermal and Electrochemical Ion Exchange Approach for Lithium Ion Batteries. *J. Mater. Chem. A* **2020**, *8*, 21289−21297.

(27) Essehli, R.; Amin, R.; Abouimrane, A.; Li, M.; ben Yahia, H.; Maher, K.; Zakaria, Y.; Belharouak, I. Temperature-dependent Battery Performance of a $Na_3V_2(PO_4)_2F_3$ Cathode and In-situ Heat Generation on Cycling. *ChemSusChem* **2020**, *13*, 5031−5040.

(28) Shen, C.; Long, H.; Wang, G.; Lu, W.; Shao, L.; Xie, K. Na3V2(PO4)2F3@C dispersed within carbon nanotube frameworks as a high tap density cathode for high-performance sodium-ion batteries. *J. Mater. Chem. A* **2018**, *6*, 6007−6014.

(29) Rui, X.; Yan, Q.; Skyllas-Kazacos, M.; Lim, T. M. $Li_3V_2(PO_4)_3$ cathode materials for lithium-ion batteries: A review. *J. Power Sources* **2014**, *258*, 19−38.

(30) Cushing, B. L.; Goodenough, J. B. Li2NaV2(PO4)3: A 3.7 V Lithium-Insertion Cathode with the Rhombohedral NASICON Structure. *J. Solid State Chem.* **2001**, *162*, 176−181.
(31) Jiang, T.; Chen, G.; Li, A.; Wang, C.; Wei, Y. Sol−gel preparation and electrochemical properties of $Na_3V_2(PO_4)_2F_3$/C composite cathode material for lithium-ion batteries. *J. Alloys Compd.* **2009**, *478*, 604−607.
(32) Feng, Q.; Peng, K.; Huang, Z.; Yan, W.; Tang, S.; Liu, Q. An Investigation of $Li_{0.6}Na_{2.4}V_2(PO_4)_2F_3$ Cathode with NASICON Structure in Lithium-Ion Battery. *J. Power Sources* **2015**, *280*, 703−709.



https://doi.org/10.1021/acsomega.2c02558
*ACS Omega* 2022, 7, 26523−26530